Efficiency Enhancement for K_α X-Ray Yields from Laser-Driven Relativistic Electrons in Solids

A. B. Sefkow, G. R. Bennett, M. Geissel, M. Schollmeier, B. C. Franke, and B. W. Atherton
Sandia National Laboratories, Albuquerque, New Mexico 87185, USA

(Received 20 December 2010; published 6 June 2011)

High-irradiance short-pulse lasers incident on solid density thin foils provide high-energy, picosecond-duration, and monochromatic K_α x-ray sources, but with limited conversion efficiency ϵ of laser energy into K_α x-ray energy. A novel two-stage target concept is proposed that utilizes ultrahigh-contrast laser interactions with primary ultrathin foils in order to efficiently generate and transport in large quantities only the most effective K_α-producing high-energy electrons into secondary x-ray converter foils. Benchmarked simulations with no free numerical parameters indicate an ϵ enhancement greater than tenfold over conventional single targets may be possible.

DOI: 10.1103/PhysRevLett.106.235002 PACS numbers: 52.38.Ph, 52.50.Jm, 52.65.Rr

High-irradiance lasers produce hot electrons in solid density thin foil targets, which generate picosecond-duration K_α x-ray emission via electron-impact ionization of the innermost shell and subsequent fluorescence [1,2]. High-energy and high-quality x-ray radiography is an essential diagnostic for high-energy-density physics (HEDP) and inertial confinement fusion experiments [3,4]. Objects with higher areal density require higher photon energies to be imaged, where the atomic number Z of the x-ray converter foil determines the K_α energy (e.g., 8–98 keV energies from Cu-U). Short-pulse laser-driven K_α sources provide nearly blur-free and monochromatic radiographic capabilities used by HEDP facilities.

The conversion efficiency ϵ of laser energy into K_α x-ray energy is a critical parameter for achieving high-brightness sources and the best imaging performance. The conventional direct-foil irradiation method using μm-sized targets ensures a small x-ray source size compatible with point-projection imaging, and peak ϵ is approximately independent of laser energy, irradiance (above 10^{18} W cm^{-2}), and target dimensions [2,5]. However, the measured efficiencies are $\epsilon = 10^{-4}$ into 4π for 25 keV K_α x-ray yields from Sn ($Z = 50$), and decrease with increasing Z [2].

Three optimized components are envisioned for the imaging system to reach its full diagnostic potential. First, devise a novel K_α x-ray source with large ϵ. Second, develop an optic with high collection efficiency and spatial resolution. Third, design an image plane detector with high sensitivity and dynamic range. Such a source *and* imaging solution may involve a large source size compatible with curved-crystal imaging, as well as allow shielding of unwanted source and object radiation. This Letter discusses the physics of the source concept.

A novel two-stage target concept is proposed that utilizes high-irradiance, ultrahigh-contrast, short-pulse laser interactions with primary ultrathin foils in order to efficiently generate relativistic electrons in large quantities. The electron cloud, ion beam, and remaining laser energy then impact a longer (~ 0.5–5 mm) secondary x-ray converter foil. Traveling at $v_e \sim c$, the hot electrons outrun the ion beam and produce K_α flux deep within the secondary target. Allowing ions to range out may contribute K_α yield through electron heating and ion impact ionization. The long converter foil needs to be optically thin in the side-on object and imager direction in order to minimize K_α photon reabsorption.

Fully explicit, kinetic, electromagnetic, and relativistic particle-in-cell simulations using the LSP code [6] are employed to model laser-target interactions self-consistently at solid density by launching laser fields from the boundary, not by prescribing an *ad hoc* injection of an assumed electron energy distribution function (EEDF). Importantly, there are no free numerical parameters. A particle-pushing routine not susceptible to the numerical Debye length instability is used. Charged particle collisions are treated. Inclusion of multiple ion charge states is found to be unnecessary because K_α yield is only weakly dependent on ionization state [7]. K_α x-ray production is computed inline from the Monte Carlo ITS code and electron-impact ionization cross sections [8]; indirect bremsstrahlung photoelectric, knock-on, and Compton electron ionization contributions to yield are neglected as minorities ($< 25\%$) in geometries of interest. This approach is in contrast to models using implicit, hybrid fluid-kinetic, or *ad hoc* EEDF injection methods, all of which inherently allow free parameters [2,5,9]. The simulation methodology has been benchmarked to direct-foil irradiation experiments using a variety of laser and target parameters. Measured ϵ varies between $\epsilon = 0.7$–2.5×10^{-4} among Sn targets, but error bars include 10^{-4} or lower. Simulated total K_α yields are within error bars and provide confidence in predictive capability.

The current understanding of direct-foil irradiation suggests ϵ cannot be substantially improved. Laser interactions with μm-sized solids produce two-temperature EEDFs with positively correlated T_{cold} and T_{hot} values. Maximum K_α yield (and ϵ) has previously been explained to occur by producing an optimal T_{hot} of a few times

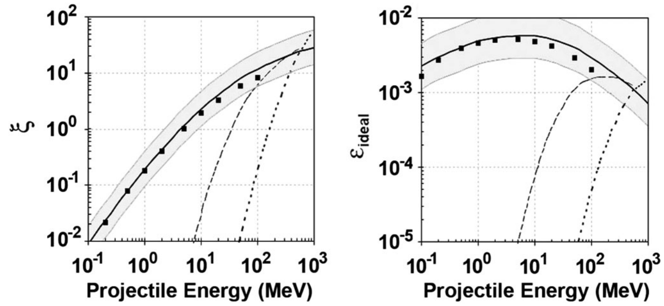

FIG. 1. The quantities ξ (left) and $\epsilon_{\rm ideal}$ (right) versus projectile energy for e^- (solid line), H^+ (dashed line), and C^{+6} (dotted line) in Sn, with e^- ITS results (squares), assuming $\rho_{\rm Sn} = 7.3\ {\rm g\,cm^{-3}}$. The gray bands illustrate the range a cumulative uncertainty factor of only 2 would introduce.

(3–6 ×) the K_α energy within a given target size using an optimal laser irradiance [10]. An optimum $T_{\rm hot}$ balances two competing effects: if $T_{\rm hot}$ is "too cold," there are too few available electrons that can ionize the K shell to produce K_α, and, if $T_{\rm cold}$ is "too hot," too much energy has been lost to bulk $T_{\rm cold}$ particles below the ionization energy (29 keV in Sn). Also, increasing $T_{\rm cold}$ blueshifts and broadens the K_α lines, and peak emissivity falls [4,5]. Reduction of ϵ at too-high energy densities during direct-foil irradiation occurs due to energy overinvestment into cold dense bulk particles.

An approximate ideal upper bound for K_α x-ray efficiency, $\epsilon_{\rm ideal}(E_e)$, from an electron of a given energy E_e within a given element can be grossly estimated. The dimensionless quantity $\xi(E_e)$ is defined as the ratio of electron range $R_e(E_e)$ to mean free path for K_α production and is roughly proportional to the number of K_α x-ray photons generated per particle from impact ionization. The $\epsilon_{\rm ideal}(E_e)$ is approximately

$$\epsilon_{\rm ideal}(E_e) \sim \xi(E_e)\, E_{K_\alpha} E_e^{-1}, \tag{1}$$

where E_{K_α} is the K_α photon energy and $E_e > E_{K_\alpha}$. The quantities ξ and $\epsilon_{\rm ideal}$ are plotted in Fig. 1 for e^-, H^+, and C^{+6}, assuming $\rho_{\rm Sn} = 7.3\ {\rm g\,cm^{-3}}$ and $n_{\rm Sn} = 3.66 \times 10^{22}\ {\rm cm^{-3}}$; comparison to monoenergetic e^- beam ITS results is provided. A broad peak in $\epsilon_{\rm ideal}(E_e)$ for Sn exists between 2–20 MeV, not a few times the K_α energy but about 80–800 × . The peak energy from this single-particle perspective is similarly high in other high-Z elements.

A number of simplifying approximations are implicit in the formula and ITS, which use cold, neutral matter cross sections and assume monoenergetic and independent particles. They do not account for uncertainties in dE/dx stopping, conduction, ionization, or straggling, or employ a self-consistent nonlocal charged particle transport model in realistic geometry. Neglected effects further include hydrodynamic expansion, photon reabsorption, indirect K_α ionization from bremsstrahlung, and electron refluxing. The gray bands in Fig. 1 illustrate the range a cumulative uncertainty factor of 2 would introduce; just the measured cold cross sections show such variation, so the uncertainty is expected to be greater. Therefore, although the upper limit on $\epsilon_{\rm ideal}$ is not certain, it may be significantly greater than tenfold above the measured 10^{-4} in the high-irradiance limit as long as relativistic MeV electrons could be very efficiently generated by the laser.

TABLE I. Electron parameters for K_α production in Sn.

E_e (MeV)	$\gamma_e\beta_e$	$n_e/n_{\rm Sn}$ (/[10^{14} W 10^{-4} cm^2])	R_e (mm)	Δt_R (ps)	$\frac{\epsilon_{\rm ideal}}{\epsilon_{0.1}}$	$\frac{\epsilon_{\rm ITS}}{\epsilon_{0.1}}$
0.5	1.71	1.318×10^{-2}	0.41	1.57	1.8	2.3
1	2.78	6.044×10^{-3}	0.97	3.44	2.2	2.7
2	4.81	2.905×10^{-3}	2.07	7.06	2.4	2.9
5	10.7	1.143×10^{-3}	4.88	16.4	2.6	3.1
10	20.5	5.695×10^{-4}	8.50	28.4	2.6	2.9
20	40.1	2.845×10^{-4}	13.6	45.5	2.3	2.5
50	98.8	1.138×10^{-4}	22.5	74.9	1.8	1.8
100	197	5.688×10^{-5}	30.1	101	1.3	1.2

The trend of $\epsilon_{\rm ideal}(E_e)$ is recovered in idealized particle simulations when one considers the injection of monoenergetic electron beams containing fixed total energy and constant power into a long Sn foil. K_α x-ray powers and total energies increase $\sim t^1$ and $\sim t^2$, respectively, during the injection time and thereafter approximately stay constant and increase $\sim t^1$, respectively. The constant x-ray power can be extrapolated to the end of the range and late-time energy dependence can be neglected because, for example, an electron with $E_e = 10$ MeV only slows to 1 MeV after traveling about 90% of its range, and $\xi(E_e)$ falls by a similar amount, indicating most of its K_α proportion has been produced. For E_e from 0.5–100 MeV, Table I provides the $\gamma_e\beta_e$ (Lorentz factor times v_e/c), density ratio $n_e/n_{\rm Sn}$ per 100 TW and 10^{-4} cm^2 of hot electrons, R_e in $\rho_{\rm Sn} = 7.3\ {\rm g\,cm^{-3}}$, and time Δt_R to range out; the final two columns show the $\epsilon_{\rm ideal}$ increase relative to the thought-to-be optimum 0.1 MeV value (4× the K_α energy) suggested by previous work and the relative ϵ increase calculated from electron beam ITS simulations.

Increased K_α production efficiency may be realized if larger quantities of relativistic electrons are generated than in typical μm-sized direct-foil irradiation, wherein MeV-level states in the EEDF are poorly occupied (typically, about a few 10^{-4} or less). The ϵ enhancement is proportional to the energy-weighted $\epsilon_{\rm ideal}$ relative increase multiplied by the relative increase in energy density content.

High-irradiance lasers produce intense ion beams from thin foils with comoving hot electron clouds providing neutralization [11]. In the ultrahigh-contrast ($\sim 10^{-12}$) and ultrathin-foil ($\sim$ 10–100 nm) regime, enhanced ion acceleration occurs with an almost entirely relativistic electron cloud [12]. High absorption levels ($> 50\%$) are attributed to relativistic transparency [13], since the laser wavelength λ_L is longer than the target Δz, which becomes comparable to the skin depth δ_p and electron Debye length $\lambda_{\rm De}$; rapid volumetric MeV-level electron heating ensues,

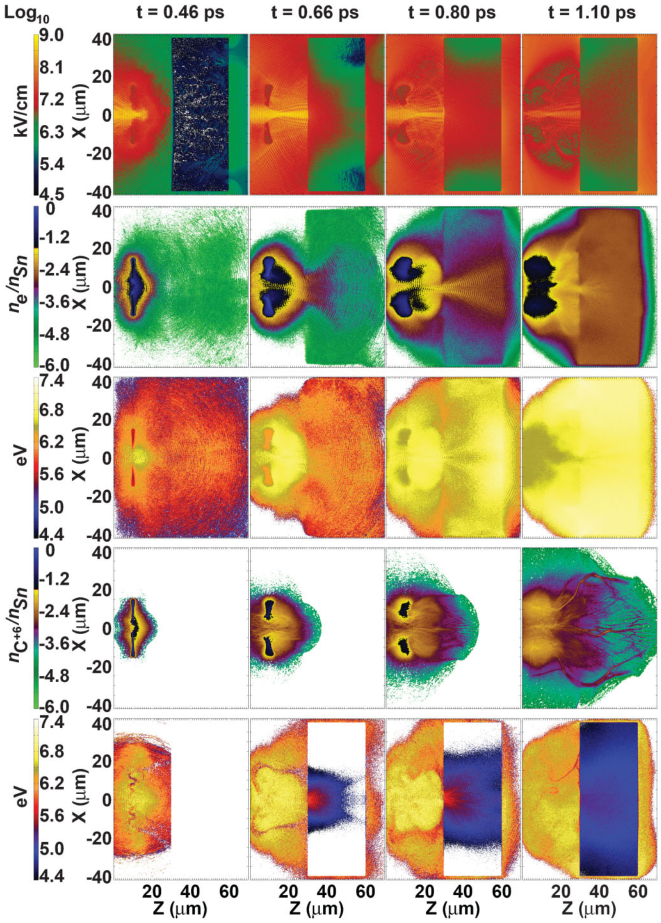

FIG. 2 (color). Integrated simulation of two-stage concept for increasing ϵ. From top to bottom: electric field magnitude; ultrathin-foil electron density, average electron energy $kT_e = \frac{2}{3}E_{\rm av}$, and ion beam density; and converter foil average electron energy are shown at $t = 0.46$, 0.66, 0.80, and 1.10 ps.

and γ_e, δ_p, $\lambda_{\rm De}$, and the critical density ($n_{\rm crit} \sim \gamma_e m_e$) all increase. The laser penetrates the relativistically underdense target and further heats essentially all electrons to MeV levels as the ions accelerate.

Simulation of the integrated two-stage concept using LSP assumes ultrahigh contrast. The $\lambda_L = 1$ μm laser energy is 120 J, with 50% energy within the Gaussian spatial and temporal FWHMs of 7 μm and 400 fs, for an averaged power and irradiance of 300 TW and $I_L \sim 5.4 \times 10^{20}$ W cm^{-2}. The linearly polarized laser strikes the ultrathin 30 μm × 90 nm C target at 0° incidence. The C foil has $\rho_{\rm C} = 2.47$ g cm^{-3} and fixed $Z = +6$, giving electron and ion densities $n_e = 6n_i = 7.38 \times 10^{23}$ cm^{-3}. The 80 × 30 μm Sn converter foil has $\rho_{\rm Sn} = 7.3$ g cm^{-3} and fixed $Z = +1$, giving equal electron and ion densities $n_e = n_i = n_{\rm Sn} = 3.66 \times 10^{22}$ cm^{-3}. The 2D Cartesian spatial extent of the grid is $x = \{-42, 42\}$ μm and $z = \{0, 70\}$ μm with $\Delta z_{\rm grid}^{\rm min} = 5$ nm near the ultrathin foil, but the nonuniform grid is larger elsewhere; the boundaries are open to both fields and particles. The ultrathin and converter foil targets are centered at $\{x, z\} = \{0, 10\}$ μm and $\{x, z\} = \{0, 45\}$ μm, respectively. The time step $\Delta t = 0.01$ fs is less than $\omega_{p,e}^{-1}$, $\omega_{c,e}^{-1}$, and $\Delta z_{\rm grid}^{\rm min}/c$. Simulation results are presented in Fig. 2.

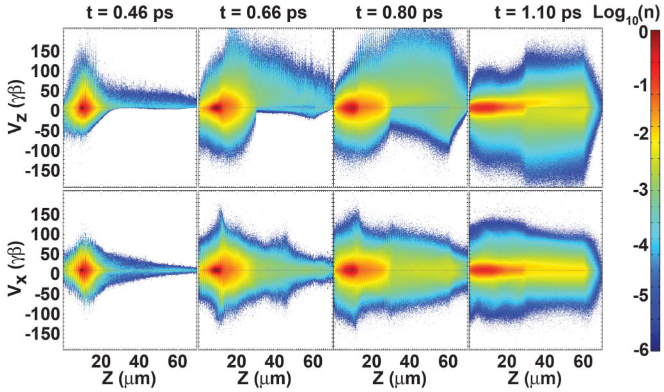

FIG. 3 (color). Ultrathin-foil electron phase space densities (normalized to Sn) at $t = 0.46$, 0.66, 0.80, and 1.10 ps. Energies E_e of 5, 10, 20, and 50 MeV are about $\gamma_e\beta_e = 10.7$, 20.5, 40.1, and 98.8. Note the nonthermal beamlike distribution.

By $t = 0.46$ ps, the laser penetrates the primary foil due to relativistic transparency: the channel is underdense even though $n_e/n_{\rm crit}^{\gamma=1}$ is about 10 because the average electron energy rises to roughly 4.5 MeV ($\gamma_e = 10$), and so $n_{\rm crit}$ also increases by 10. Some low-density hot electrons have already encountered the x-ray converter foil.

By $t = 0.66$ ps, the intense ion beam strikes the secondary target. Ultrathin-foil electrons are in transit with increasing densities, and undergo continued heating into the 2–25 MeV average energy range. The remaining laser energy heats converter foil hot electrons on the axis and underdense blow-off plasma between the two foils; it also self-focuses due to the relativistic electrons [14] and increases the effective irradiance at the secondary target.

By $t = 0.80$ ps, the ultrathin-foil electrons are achieving higher densities and 5–25 MeV average energies within the secondary target, whose on-axis hot electrons are heated to 0.1–1 MeV levels. The $\Delta z = 30$ μm converter foil is too short to recover much ion beam energy, only C^{+6} ions with <45 MeV will stop within the Sn.

By $t = 1.10$ ps, laser heating ends but ultrathin-foil electrons continue to enter and recirculate in the secondary target with 5–25 MeV average energies and high densities between $n_e/n_{\rm Sn} \sim 0.1–1 \times 10^{-2}$. Converter foil hot electrons have K_α-relevant 75–300 keV average energies.

Normalized ultrathin-foil electron phase space densities are shown in Fig. 3. The primary target electrons within the converter foil at $t \geq 0.8$ ps have a nonthermal beamlike distribution and are essentially all above 2 MeV; the energy majority is carried by 5–25 MeV electrons (the peak is 10 MeV) with high relative density. The most efficient MeV-level states are populated by greater than 20-fold relative to direct-foil irradiation, resulting in significantly improved K_α x-ray production efficiency.

Figure 4 provides the laser and K_α x-ray powers and energies from the integrated two-stage particle simulation.

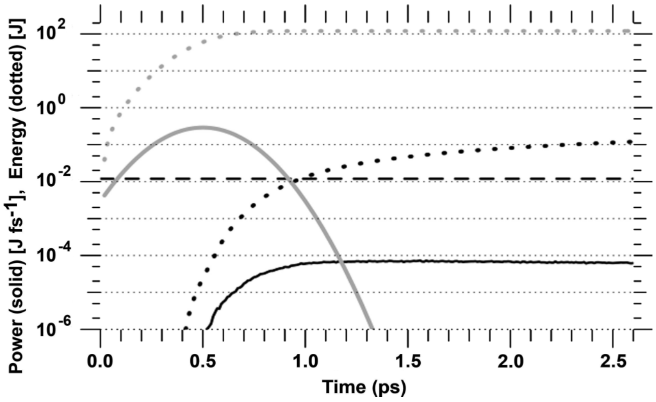

FIG. 4. Laser (gray) and K_α x-ray (black) power in J fs^{-1} (solid lines) and energy in J (dotted lines). The dashed line denotes 10^{-4} efficiency relative to the laser energy. By $t = 2.6$ ps, the efficiency is tenfold higher than direct-foil irradiation.

The total x-ray power rises to about 70 mJ ps^{-1} around $t = 1.2$ ps and thereafter stays nearly constant, an increase of over 20-fold relative to the conventional method. By $t = 2.6$ ps, an ϵ enhancement of tenfold is simulated ($\epsilon = 10^{-3}$) and the x-ray power is still high. However, the simulated converter foil length of 30 μm is suboptimal and K_α power would fall prematurely; in addition, ion beam contributions increase in time but are underestimated herein. This simulation uses 10^5 time steps ps^{-1}, $\sim 10^9$ particles, $\sim 10^7$ grid nodes, and 3 days ps^{-1} on about 1000 processors. It is not yet feasible to scale up by factors of 10 in both space and time in order to predict the final ϵ enhancement, but it may significantly exceed tenfold by the time K_α x-ray production stops in a longer foil. The x-ray production may be conservatively estimated to cease around $t = 30$ ps, the associated time to range out for the most-populated 10 MeV electron level.

The upper bound on achievable ϵ depends on the optimized matching of target parameters to the laser system, the total conversion efficiency of the laser into useful K_α-producing energy (> 29 keV in Sn), and the uncertainties mentioned earlier. The ultrathin target dimensions should be matched to the laser energy and duration, and the element choice is a design parameter. The separation distance between the targets must be optimized to achieve sufficient ion acceleration and electron heating while avoiding loss of coupling to the secondary target. Recovery of ion beam energy in long targets can occur through deposition into electrons or direct impact ionization. Remaining laser energy can be self-focused to higher irradiance, which then produces hotter secondary target electrons. Total conversion efficiency of laser energy into useful charged particle energy in two-stage designs can be 65%–85% in simulations, when absorption into all ultrathin and secondary target particles is taken into account, and significantly less energy is wasted to reflection and electron energies below the K_α threshold. The required $\sim 10^{-12}$ level of ultrahigh-contrast to prevent premature melt of ultrathin targets has been recently achieved (cf. Henig *et al.* [12]). In summary, by accelerating bulk electrons from ultrathin foils rather than just high-energy tails during direct-foil irradiation, the two-stage concept enables high-ϵ x-ray sources of user-chosen K_α energies using much less laser energy.

Sandia is a multiprogram laboratory operated by Sandia Corporation, a Lockheed Martin Company, for the National Nuclear Security Administration under Contract No. DE-AC04-94AL85000. Support provided by the Laboratory Directed Research and Development Program at Sandia. The authors acknowledge M. C. Herrmann, C. W. Nakhleh, and J. L. Porter for support, S. B. Hansen, D. B. Sinars, and S. Swanekamp for feedback, and R. B. Campbell, R. P. Kensek, and D. R. Welch for code support.

---

[1] J. D. Hares *et al.*, Phys. Rev. Lett. **42**, 1216 (1979); H. M. Milchberg, I. Lyubomirsky, and C. G. Durfee, *ibid.* **67**, 2654 (1991); S. C. Wilks *et al.*, *ibid.* **69**, 1383 (1992).
[2] H. Chen *et al.*, Phys. Rev. Lett. **70**, 3431 (1993); A. Rousse *et al.*, Phys. Rev. E **50**, 2200 (1994); S. N. Chen *et al.*, Phys. Plasmas **14**, 102701 (2007); P. Neumayer *et al.*, High Energy Density Phys. **5**, 244 (2009).
[3] G. R. Bennett *et al.*, Phys. Rev. Lett. **89**, 245002 (2002); B. E. Blue *et al.*, *ibid.* **94**, 095005 (2005); G. R. Bennett *et al.*, *ibid.* **99**, 205003 (2007); S. X. Hu *et al.*, *ibid.* **100**, 185003 (2008); E. C. Harding *et al.*, *ibid.* **103**, 045005 (2009); D. B. Sinars *et al.*, *ibid.* **105**, 185001 (2010).
[4] H.-S. Park *et al.*, Phys. Plasmas **13**, 056309 (2006); H.-S. Park *et al.*, *ibid.* **15**, 072705 (2008).
[5] J. Myatt *et al.*, Phys. Plasmas **14**, 056301 (2007); P. M. Nilson *et al.*, *ibid.* **15**, 056308 (2008); P. M. Nilson *et al.*, Phys. Rev. E **79**, 016406 (2009).
[6] T. P. Hughes, R. E. Clark, and S. S. Yu, Phys. Rev. ST Accel. Beams **2**, 110401 (1999). LSP is a software product developed by ATK Mission Research, Albuquerque, NM 87110.
[7] R. C. Kirkpatrick (private communication).
[8] A. Halbleib *et al.*, IEEE Trans. Nucl. Sci. **39**, 1025 (1992); M. A. R. Patoary *et al.*, Int. J. Quantum Chem. **108**, 1023 (2008); http://physics.nist.gov/; http://srim.org.
[9] R. B. Stephens *et al.*, Phys. Rev. E **69**, 066414 (2004); R. J. Mason, E. S. Dodd, and B. J. Albright, *ibid.* **72**, 015401(R) (2005); W. Theobald *et al.*, Phys. Plasmas **13**, 043102 (2006); C. T. Zhou *et al.*, *ibid.* **17**, 083103 (2010).
[10] Ch. Reich *et al.*, Phys. Rev. Lett. **84**, 4846 (2000); F. Ewald *et al.*, Europhys. Lett. **60**, 710 (2002); D. Salzmann *et al.*, Phys. Rev. E **65**, 036402 (2002).
[11] R. A. Snavely *et al.*, Phys. Rev. Lett. **85**, 2945 (2000); P. Mora, *ibid.* **90**, 185002 (2003); B. J. Albright *et al.*, *ibid.* **97**, 115002 (2006).
[12] L. Yin *et al.*, Laser Part. Beams **24**, 291 (2006); L. Yin *et al.*, Phys. Plasmas **14**, 056706 (2007); A. Andreev *et al.*, Phys. Rev. Lett. **101**, 155002 (2008); A. Henig *et al.*, *ibid.* **103**, 045002 (2009).
[13] E. Lefebvre and G. Bonnaud, Phys. Rev. Lett. **74**, 2002 (1995); J. Fuchs *et al.*, *ibid.* **80**, 2326 (1998).
[14] P. Monot *et al.*, Phys. Rev. Lett. **74**, 2953 (1995).